Structural Engineering and Mechanics, *Vol. 74, No. 6 (2020) 771-787*
DOI: https://doi.org/10.12989/sem.2020.74.6.771

Uncertainties in blast simulations evaluated with Smoothed Particle Hydrodynamics method

Martin Husek* and Jiri Kala[a]

Institute of Structural Mechanics, Faculty of Civil Engineering, Brno University of Technology, Veveri 331/95, 602 00 Brno, Czech Republic

(Received November 18, 2019, Revised January 30, 2020, Accepted January 31, 2020)

Abstract. The paper provides an inside look into experimental measurements, followed by numerical simulations and their related uncertainties. The goal of the paper is to present findings related to blast loading and the handling of defects that are inherent in experiments. Very often it might seem that experiments are simplified reflections of real-life conditions. In most cases this is true, but there is a good reason for that. The more complex an experiment is, the larger the amount of uncertainties that can be expected. This especially applies when the blast loading of concrete is the subject of research. When simulations fail to reproduce the results of experimental measurements, it does not necessarily mean there is something wrong with the numerical model. The problem could be missing information. Put differently, the numerical simulation may lack information that seemed irrelevant with regard to the experiment. In the presented case, a reference simulation with a proven material model unexpectedly failed to replicate the results of an experiment where concrete slabs were exposed to blast loading. This resulted in a search for possible unknowns. When all of the uncertainties were examined, the missing information turned out to be the orientation of the charge to the concrete slab. Since the experiment was burdened with error, a sensitivity study had to take place so the influence of this factor could be better understood. The findings point to the fact that even the smallest defect during experiments must somehow be taken into account when designing numerical simulations. Otherwise, the simulations are not correlated to the experiments, but merely to some expectations.

Keywords: blast loading; metamodels; sensitivity study; Smoothed Particle Hydrodynamics; uncertainties

1. Introduction

When experiments are simulated, it is very often necessary to perform calibrations. This middle step takes quite an amount of time. However, when the calibrations are finished and the simulation has been calibrated, much more information can be extracted from it than from the experiment itself. This is due to the fact that it is not always possible to measure all responses during an experiment. For example, it is almost impossible to locate crack development inside a concrete specimen. In simulations, on the other hand, plastic deformations can be tracked very easily and can provide a good estimate of crack development location. However, experiments are not influenced by artificial numerical errors. Experiments and simulations can be considered to be tools for researchers. Each of them can provide a certain level of information.

What is very often overlooked is the link between them. The link is nothing other than the selected information which is taken from experiments and considered in simulations. When an excessive amount of information is taken from experiments and has to be somehow reflected in simulations, the resultant simulations tend to be over-constrained. In other words, the variation window for the simulations is very small and calibration often fails. In the opposite scenario, when too little information is taken from experiments, several simulation variants can result in a successfully calibrated case, which is not desirable – a unique solution is required, or worse, calibration fails due to the presence of many uncertainties.

The paper presents a case when experimental measurements preceded simulations. The experiment involved the blast loading of reinforced concrete slabs. The response of the concrete in terms of dynamic and static displacement, strain and damage was measured. All the responses from the experiment were used as the foundation stone for numerical simulations in which material development should take place. The only variable in the experiment was the distance between the charge and the concrete slab. When all the experimental measurements were finished, a numerical model was created in LS-DYNA (LSTC 2019a).

From the early results with the previously calibrated and well tested material model (Husek and Kala 2018, Murray 2007, Murray *et al.* 2007) it was obvious that the responses dramatically differed from those obtained from the experiments. The first thought was, of course, that numerical error was to blame, e.g. an inconsistent unit system. The material model and the calibrated input parameters were again tested in simulations based on similar experiments (Codina *et al.* 2016). The results supported the assumption that the material parameters had been calibrated well. Sensitivity studies and robustness analyses were eventually carried out to further evaluate the model. Neither the material parameters nor the numerical

*Corresponding author, Ph.D. Student
E-mail: husek.m@fce.vutbr.cz
[a] Associate Professor
E-mail: kala.j@fce.vutbr.cz

http://www.techno-press.com/journals/sem&subpage=7
ISSN: 1225-4568 (Print), 1598-6217 (Online)

model were burdened with error. Since the measured data from the experiments seemed to be as expected, the only possible explanation was that there must be uncertainty in the link between the experiment and the simulation, and indeed there was.

The concrete slabs and their behaviour during the explosion were monitored quite well. Laser sensors, strain gauges and a high-speed camera were used. Unfortunately, too little attention was paid to the charge itself. A detailed description of the experiment can be found below after the *Introduction* section. However, for the sake of the completeness of this section it is important to mention that the charge was of cylindrical shape. It was not special, just standard military explosive. The distance between the charge and concrete slab was always double-checked. The orientation of the charge, however, was not. Evaluated retrospectively, the orientation plays a significant role even with smaller charges. Blast loading experiments are considered to be particularly challenging to perform. Difficulties are always present, and it does not matter if the blast loading is being imposed on slabs (Rashad *et al*. 2019, Rashad and Yang 2019, Wua *et al*. 2019, Luccioni *et al*. 2017, Ruggiero *et al*. 2019, Yun *et al*. 2013), walls (Sohn *et al*. 2014, Jin-Won *et al*. 2016, Shi and Stewart 2015, Xiao *et al*. 2019, Zhan *et al*. 2019, Jina *et al.* 2019) or columns/beams (Han-Gul and Hyo-Gyoung 2017, Tuan and Priyan 2009, Yuan *et al*. 2017, Lin *et al*. 2019, Jun and Hong 2014). There are problems which must be overcome.

When blast loading is modelled, several approaches can be used to simulate the blast wave. The very first choice because of its simplicity is usually the empirical approach referred to as ConWep (US Army 1986, US Army 1990) or just simply the 'pressure projection' method (Le Blanc *et al*. 2005, Schwer 2010, Schwer *et al.* 2015). As the name suggests, the empirically calculated pressure is directly mapped onto the outer surface of the loaded specimen. The pressure is a function of time, and since the pressure applied to the model corresponds to a directly given value it is possible to capture the positive phase of the blast wave (overpressure), as well as the negative phase (suction). Unfortunately, there is no information about the shape of the charge and it is not possible to simulate possible reflections and interferences of the blast wave (even though direct reflection from the loaded surface can be included as a multiplier of the incident pressure). With the pressure projection method, it is enough to have a certain amount of knowledge about the Lagrangian Finite Element Method (FEM) and structural mechanics. With more complex methods, however, the required knowledge is much greater.

The most versatile method for blast simulations is without question combined Lagrangian/Eulerian FEM. In LS-DYNA terminology it is known as the Multi-Material Arbitrary Lagrangian Eulerian method (MM-ALE) (Schwer 2010, Schwer *et al.* 2015, Slavik 2009, Trajkovski 2017). Detonation products, air and other fluids are simulated with an Eulerian domain where material flows through a computational mesh. The structural parts of the model are simulated with Lagrangian elements where the material deforms with the mesh. The interaction between both domains is handled with coupling algorithms, e.g. penalty or constraint-based methods. These are very often referred to as Fluid Structure Interaction algorithms (FSI). Blast wave reflections, interference, shape of charge and overall complex behaviour can be captured. Computational time and knowledge of the involved methods and coupling algorithms are needed, however.

Since ConWep and MM-ALE are very often combined with Lagrangian elements, it is in place to remind the biggest disadvantage of the mesh or grid-based methods – the computational mesh itself (Husek and Kala 2016, Liu 2003, Liu and Liu 2010). As elements undergo excessive deformations, simulation results tend to be burdened with numerical errors (shear/volumetric locking, hourglass effect, negative volume). Highly distorted elements can also negatively influence time step of the simulation, therefore, computational time further increases. How to remove problematic elements from the simulation is another question. Element erosion technique is very often used. Unfortunately, there is no general rule what should be the erosion limit (Luccioni and Aráoz 2011, Husek and Kala 2016). When fracture growth in brittle material is expected, size of the elements is another issue (Codina *et al*. 2016). Based on the element size, the element erosion can lead to unstable propagation of the crack. Yet there is another issue – element orientation. It was proven that fracture propagation in structured meshes requires less fracture energy than in case with unstructured/free meshes (Will and Eckardt 2017, Will *et al*. 2017). That being said, need for new numerical methods and approaches for blast simulations is justified.

Blast waves can be simulated with meshfree particle methods. Many methods have been developed over the years and there are plenty to choose from, e.g. the Smoothed Particle Hydrodynamics method (SPH), the Discrete Element Method (DEM), the Corpuscular Particle Method (CPM) and the CPM-based Particle Blast Method (PBM). It is important to realize that methods like SPH and DEM were not developed directly for gas flow modelling. On the other hand, methods like CPM were actually developed for gas flow modelling, but only for when the flow is slow. When particles discretize explosive material and subsequently approximate detonation products, the fact that the material can be tracked very easily and therefore provide a great amount of information is the biggest advantage. The air domain should always be simulated if possible (Schwer *et al.* 2015). In some cases where the air domain can be omitted, e.g. close-in detonations (Toussaint and Durocher 2008, Hilding 2016) or buried charges (Toussaint and Bouamoul 2010, Barsotti 2012, Barsotti *et al*. 2016, Chen and Lien 2018, Kurtoglu *et al*. 2013) and particles are only used for the discretization of explosive material, the negative phase cannot be captured. For close-in detonations, however, the suction phase is not so important, especially when smaller charges are used.

When only blast loading is being analysed, the presence of a target, or concrete slab in this particular case, is not actually necessary. Since only the effect of the blast is of interest, only the top surface of the concrete needs to be taken into account. The pressure distribution, time of blast wave arrival and even the unbalanced force moment from

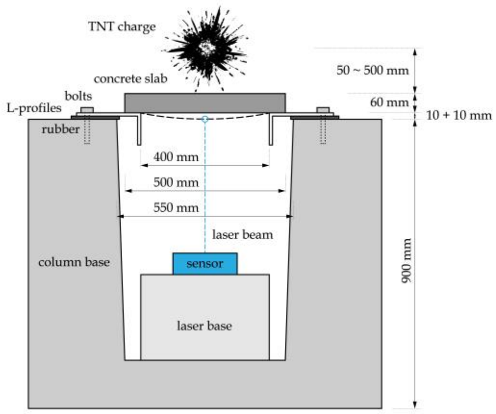

Fig. 1 Schema of the experiment configuration

Fig. 2 The experiment configuration

the pressure distribution and more can be easily extracted with just a rigid surface as a sensor. In the presented case the SPH method was chosen for blast modelling and Lagrangian shell FEM elements for the sensor modelling. The sensor ultimately represents the top surface of the concrete slab. From the overall point of view, the SPH method was able to simulate the aforementioned defect with the rotated charge and evaluate its influence. The results point to the fact that even though the defects in the experimental measurements were discovered retrospectively, they must have been somehow reflected in the numerical simulations.

2. Experiment

The experiment was designed to be robust, modular and as simple as possible. A schema of the experiment configuration is in Fig. 1. Since the effect of the explosion is the topic of the paper, what follows is only a brief description of the real experiment.

2.1 Configuration

The tested concrete slabs were freely placed on a supporting structure consisting of a concrete column base.

Table 1 Charge specifications

material	TNT
shape	cylinder
m	75 g
d	30 mm
l	70 mm
ratio of *l* to *d*	2.33

Fig. 3 The placed charge before detonation

Because the equipment is to be reused in future experiments with a variety of slab sizes, a steel structure made from L-profiles was placed between the slabs and the column base. With this secondary structure, the size of the column base hole can be reduced, allowing smaller slabs to also be tested. Between the column base and the steel structure a layer of hard rubber was added. The reason for that was explosive energy accumulation. Without the rubber layer, the top surface of the column base would be damaged after every nth explosion. The steel structure was connected to the column base with four bolts. The bolt tightening force was significant; therefore, the whole system was considered to be prestressed. The concrete slabs (dimensions 500 mm x 500 mm x 60 mm) were lightly reinforced in the middle. C30/37 concrete and B500 steel were used, as defined by Eurocode standards. The reinforcement was standardized 6 mm diameter rebar reinforcing wire mesh with 100 mm spacing. In other words, there were five rebars in each direction. An overall image of the configuration of the experiment is shown in Fig. 2.

2.2 Charge

The charge was placed above each concrete slab. The distance between the top surface of the slab and the lowest point of the charge varied from 50 mm to 500 mm as it was the independent variable. The charge was a standard engineering Trinitrotoluene (TNT) charge of cylindrical shape. The specifications of the charge are summarized in Table 1, where *m*, *d* and *l* stand for the mass, diameter and length of the charge, respectively. A close-up view of a properly placed and fixed charge is shown in Fig. 3.

Fig. 4 Laser sensor inside the column base protected with Plexiglass

Fig. 5 Strain gauge placed on the top surface of the concrete slab

The charge was fixed in place with wires. For this purpose, a wooden tripod was built as shown in Fig. 2. Vertical fixation was controlled by a wire leading from the topmost point of the tripod. Horizontal fixation was controlled by wires leading from the tripod's legs, which is clearly visible in Fig. 3.

2.3 Gauges

An optoNCDT laser sensor was used for dynamic displacement measurement in the centre of the slabs. It was placed inside the column base, as shown in Fig. 1. A protective shield made from Plexiglass was placed directly above the sensor to prevent concrete debris from causing any damage. A view inside the column base after 'detonation calibration' (a preliminary explosion) had taken place is shown in Fig. 4. The strain gauges were placed on the top and bottom surface of the slabs based on the detonation distance. Placement on the top surface is shown in Fig. 5.

2.4 Observations

After the experiment was finished and all measurements had been stored, some observations were made. Not all the concrete slabs were blackened in the same way. It did not seem to be important at that point.

To elaborate further, when a charge has a certain shape and is initiated (detonated) from a certain point, a detonation wave propagates from this point through the explosive and releases energy. Based on the shape of the charge and on the detonation point location, the detonation product distribution and pressure field differ. Since it was not the researchers' intention to record detonations with a high-speed camera but rather to investigate the behaviour of the concrete slabs, information about the detonation product distribution is not available. The position of the camera was too far from the detonation and the recording frequency was too low to provide such data. Nevertheless, it is still possible to observe the detonation product distribution from the blackened pattern on the concrete slabs.

3. Problem definition

When the simulations started and a representative case with a charge distance of 100 mm was calculated, it seemed that the applied force in the simulation was completely off the scale, i.e. it was simply too high. Furthermore, from the measured responses it was obvious that the pressure distribution, (and thus peak pressure) was not centred at all. After the photo documentation had been analysed again, there was no question that the blackened patterns and the rotation of the charges were somehow correlated. The observations led to the formulation of the following theory. When a cylindrical charge detonates, a pressure field is formed and propagates through the air from the detonation point. Due to the shape of the charge, the pressure field is not spherical. When the detonation point is in the centre of the cylinder, the pressure peak of the formed pressure field is expected either on the axis of symmetry of the cylinder or in the plane parallel to the cylinder base passing through the detonation point. To determine where the peak pressure may be, the ratio of the cylinder's length to its diameter has to be taken into account. Regardless of what the ratio is, when the axis of the cylinder is not perpendicular to the concrete slab surface, three things happen. First, the loading is not symmetrical, which results in additional applied force moments. Second, the pressure peak is smaller since the blast wave is not reflected from the surface in exactly the opposite direction but rather at a certain angle. And third, the boundary conditions play a more important role since the resulting force is moving from the centre to the boundaries.

3.1 Correct charge placement

In an ideal case the base of the cylindrical charge is parallel to the concrete slab surface. After the explosion, the applied pressure field is radially symmetrical and centred on the axis of symmetry of the concrete slab. The resultant force of the pressure field is therefore located at the centre of the concrete slab and is normal to the surface. Furthermore, the summation of force moments is zero since the applied forces are symmetrical. The blackened pattern

Fig. 6 Blackened pattern from the explosion (adjusted contrast)

Fig. 7 Incorrectly placed charge

should correspond to the aforementioned characteristics, i.e. it is symmetrical and centred on the slab centre. Illustrations depicting correct charge placement and a proper (expected) blackened pattern are shown in Fig. 3 and Fig. 6, respectively. It is obvious that the blackened pattern is more or less centred and fades out from the centre smoothly. This supports the fact that the charge was centred and the axis of the charge was perpendicular to the concrete slab.

3.2 Incorrect charge placement

When the charge is placed incorrectly, i.e. rotated or shifted from the centre of the slab, an asymmetrical pressure distribution field, a smaller peak pressure and more or less random damage to the slab can be expected. Such a placement is shown in Fig. 7. It is obvious that the charge axis is not perpendicular to the concrete slab surface. Even though it is quite easy to see that something is wrong in the photo, it is very problematic to observe such a deviation during the experiment. The incorrect charge placement may result in an asymmetrical blackened pattern, as shown in Fig. 8. Several points can be made about the pattern in this particular case. The imaginary centre of the pattern is not aligned on the centre of the concrete slab. Furthermore, the imaginary principal axes of the pattern distribution tend to rotate. This probably means that the rotation of the charge was spatial, i.e. around two imaginary axes.

Fig. 8 Blackened pattern from the explosion of an incorrectly placed charge (adjusted contrast)

3.3 Deviation quantification

Let us specify the terminology required to quantify the rotations of the charge. In Fig. 9 the zenith, the azimuth and their corresponding angles are defined on a celestial sphere. The Z axis represents the zenith. The angle between a direction of interest (e.g. vector **r**) and the zenith is zenith angle Φ. The X and Y axes represent the horizontal plane (e.g. the top surface of the concrete slab). The angle between the X axis and the direction of interest projected into the XY plane is azimuth angle θ. Since the X, Y and Z axes are not important in this particular case, the zenith angle and azimuth angle will be further referred to as the zenith and azimuth for short. The celestial sphere or unit sphere and its origin can be placed in the centre of gravity of the charge, which is also the detonation point. Vector **r** then corresponds to the axis of the charge. The larger the zenith and azimuth are, the greater the deviation from the intended experiment.

4. Numerical simulation

Quite an amount of simulations must be calculated in order to analyse the variation in an input parameter – initial rotational deviation of the charge in this particular case. However, since only the effect of the blast is being evaluated rather than damage to the concrete slabs, the model created in LS-DYNA was relatively simple. Instead of a detailed model of the reinforced concrete slab, only the top surface was constructed, using FEM shell elements. The sole purpose of this layer of elements was to measure the applied pressure from explosions, i.e. to act as a sensor recording pressure distribution over time. The behaviour of the sensor was, therefore, rigid. The easiest way to evaluate the overall loading effect is to calculate the summation of all applied forces. This was done with a predefined boundary condition. When a rigid body is used, only one constrained node can be defined. In this particular case, the centre node corresponding to the centre of gravity of the sensor was constrained. In other words, all translational and rotational degrees of freedom were fixed. With this approach, not only the total reaction force can be measured, but also its components, force moment components and total force moment as well. When all of the six reaction components are available, a very good picture of unsymmetrical pressure distribution can be created. To capture peak pressure, a very fine mesh of 10,000 elements was used.

4.1 Blast loading

The charge itself was modelled in detail with the SPH method. No simplification was performed. Over 100,000 particles were generated for every calculated simulation. Initial particle distribution was based on uniform Cartesian grid where distance between particles was 0.75 mm. Particles outside the charge volume were simply removed. With particle spacing of 0.75 mm, volume assigned to one particle was approx. 0.5 mm^3. This approach is recommended for the most of the SPH simulations (Husek and Kala 2018, LSTC 2019a). The dimensions of the charge have already been mentioned in Table 1. The high explosive burn material model (LSTC 2019b) and Jones–Wilkins–Lee (JWL) equation of state (LSTC 2019b, Baker 1991) for TNT were used. The material parameters and equation of state parameters are listed in Table 2 and Table 3, respectively. The JWL equation of state specifies the relation between pressure and volume, or rather density, of the detonation products as

$$p_{eos} = A\left(1-\frac{\omega}{R_1 V}\right)e^{-R_1 V} + B\left(1-\frac{\omega}{R_2 V}\right)e^{-R_2 V} + \frac{\omega E}{V}, \tag{1}$$

where relative volume V is defined as the ratio of detonation product volume v to the initial volume of explosive v_0, or as the ratio of initial explosive density ρ_0 to detonation product density ρ, as follows:

$$V = \frac{v}{v_0} = \frac{\rho_0}{\rho}. \tag{2}$$

The detonation (initial) energy per unit volume E specifies how much energy is released. To calculate the detonation energy of explosive for a particular case, the initial volume of the charge is needed. The rate of detonation energy release is controlled by the material model. The outcome of the high explosive burn material model is termed 'burn fraction F', which specifies how much of the material detonated. The burn fraction multiplies the equation of state pressure and gives the pressure available to the system as

$$p = F p_{eos}. \tag{3}$$

F is a function of the initial explosive density ρ_0, the detonation velocity D and Chapman–Jouguet pressure p_{CJ}.

As previously mentioned, the air domain was not simulated. The distance between the sensor and the bottom surface of the charge was always 100 mm, as in the representative case. The centre of gravity of the charge (which is also the detonation point) was always aligned to the centre of the sensor. Although it will be discussed later, an overview of a few simulations (designs), including three 'boundary designs' and design 76, is shown in Fig. 10. Before embarking on a complex description of the involved variables, here is a brief review of the SPH method.

Table 2 High explosive burn material model parameters for TNT

ρ_0	1,515 kgm^{-3}
D	6,930 ms^{-1}
p_{CJ}	21 GPa

Table 3 Jones–Wilkins–Lee equation of state parameters for TNT

A	373.8 GPa
B	3.747 GPa
R_1	4.15
R_2	0.90
ω	0.35
E	7 GJm^{-3} or GPa

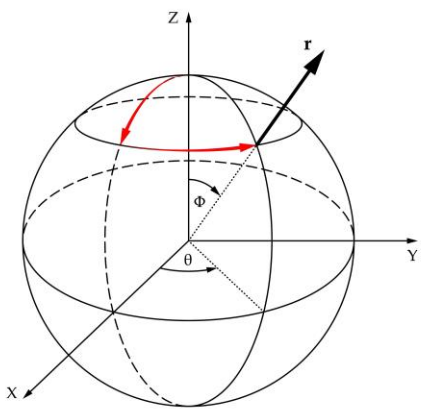

Fig. 9 Azimuth – θ, and zenith – Φ definition

4.2 The SPH method

The mathematical background and main idea of the SPH method are comprehensively described in (Monaghan 1992, Liu and Liu 2003, Liu and Liu 2010, Liu 2010) and therefore only a brief review of the essential theory follows. The formulation of the SPH method can be divided into two steps: the integral representation of field functions, and particle approximation. The concept of the integral representation of a function $f(\boldsymbol{x})$ starts from the following identity:

$$f(\boldsymbol{x}) = \int_{\Omega} f(\boldsymbol{x}')\delta(\boldsymbol{x}-\boldsymbol{x}')d\boldsymbol{x}', \tag{4}$$

where f is a function of the three-dimensional position vector $\boldsymbol{x}$, and δ $(\boldsymbol{x} - \boldsymbol{x}')$ is the Dirac delta function. The

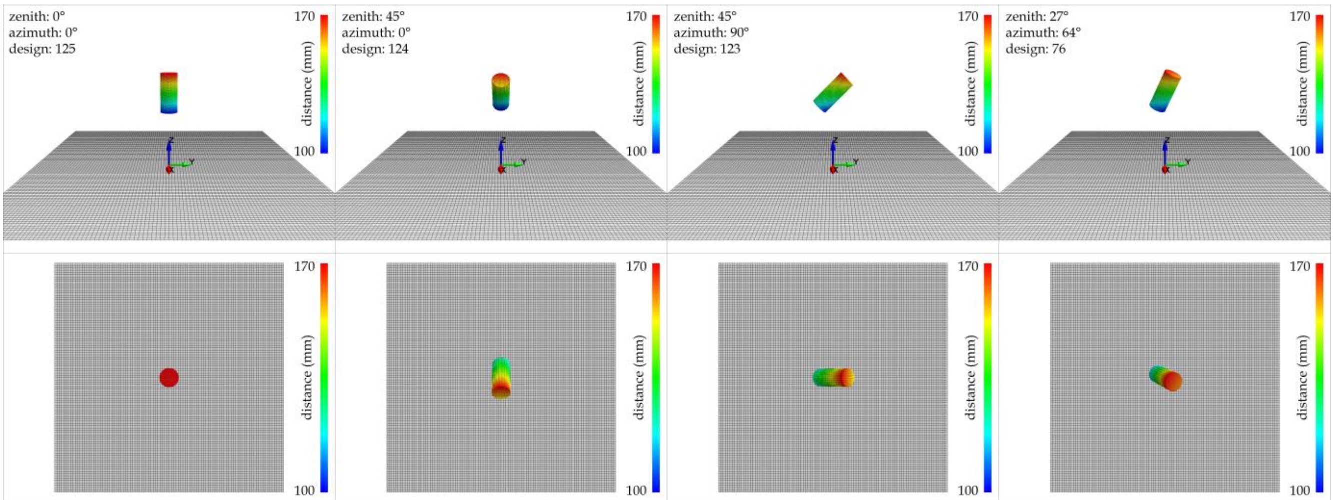

Fig. 10 Numerical simulation overview of three boundary designs (from left) and design 76 (right). Plotted particle distance from the global coordinate system; iso and top view

Dirac delta function can be understood in many forms, e.g. as a line which is zero everywhere except at $\boldsymbol{x}$, where it is infinite:

$$\delta\left(\boldsymbol{x}-\boldsymbol{x}'\right)=\begin{cases}\infty, & \boldsymbol{x}=\boldsymbol{x}',\\ 0, & \boldsymbol{x}\neq\boldsymbol{x}',\end{cases} \tag{5}$$

and therefore, it must be constrained to satisfy the identity

$$\int_{\Omega}\delta\left(\boldsymbol{x}-\boldsymbol{x}'\right)d\boldsymbol{x}'=1. \tag{6}$$

In Eq. (5), $\boldsymbol{\Omega}$ is the volume of the integral that contains $\boldsymbol{x}$. Eq. (5) implies that a function can be represented in an integral form (Liu and Liu 2003). Since the Dirac delta function is used, the integral representation in Eq. (5) is exact or rigorous as long as $f(\boldsymbol{x})$ is defined and continuous in $\boldsymbol{\Omega}$ (Liu and Liu 2003). If the Delta function $\delta\ (\boldsymbol{x}-\boldsymbol{x}')$ is replaced by a smoothing function $W(\boldsymbol{x}-\boldsymbol{x}', h)$, the integral representation of $f(\boldsymbol{x})$ is given by

$$f\left(\boldsymbol{x}\right)\approx\int_{\Omega}f\left(\boldsymbol{x}'\right)W\left(\boldsymbol{x}-\boldsymbol{x}',h\right)d\boldsymbol{x}', \tag{7}$$

where W is the 'smoothing function' and h is the smoothing length defining the influence area of the smoothing function W. Note that as long as W is not the Dirac delta function, the integral representation in Eq. (7) can only be an approximation (Liu and Liu 2003). The smoothing function W has to fulfil certain conditions. At this moment, the normalization condition can be considered to be

$$\int_{\Omega}W\left(\boldsymbol{x}-\boldsymbol{x}',h\right)d\boldsymbol{x}'=1, \tag{8}$$

which was also stated in Eq. (6). The continuous integral representations concerning the SPH integral approximation in Eq. (7) can be converted into discretized forms of summation over all the particles in the support domain shown in Fig. 11. The corresponding discretized process of summation over the particles is commonly known as particle approximation.

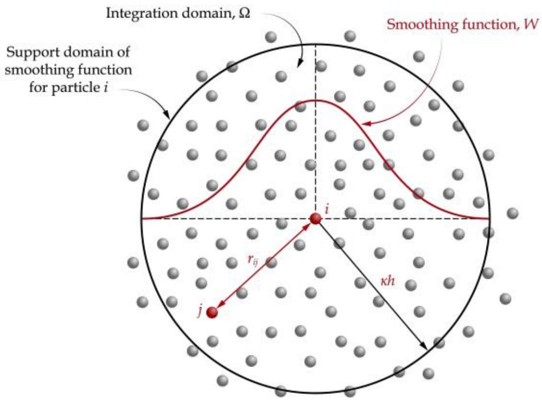

Fig. 11 Particle approximation of the SPH method

If the infinitesimal volume $d\boldsymbol{x}'$ in Eq. (7) at the location of particle j is replaced by the finite volume of the particle ΔV_j that is related to the mass of the particles m_j by

$$m_j=\Delta V_j\rho_j, \tag{9}$$

where ρ_j is the density of particle j in the support domain of particle i, then the continuous SPH integral representation for $f(\boldsymbol{x})$ can be written in the following form of discretized particle approximation (Liu and Liu 2003) as

$$\begin{aligned} f\left(\boldsymbol{x}\right)&\approx\int_{\Omega}f\left(\boldsymbol{x}'\right)W\left(\boldsymbol{x}-\boldsymbol{x}',h\right)d\boldsymbol{x}',\\ &\approx\sum_j f\left(\boldsymbol{x}_j\right)W\left(\boldsymbol{x}-\boldsymbol{x}_j,h\right)\Delta V_j,\\ &\approx\sum_j f\left(\boldsymbol{x}_j\right)W\left(\boldsymbol{x}-\boldsymbol{x}_j,h\right)\frac{1}{\rho_j}\left(\rho_j\Delta V_j\right),\\ &\approx\sum_j f\left(\boldsymbol{x}_j\right)W\left(\boldsymbol{x}-\boldsymbol{x}_j,h\right)\frac{1}{\rho_j}\left(m_j\right),\\ &\approx\sum_j\frac{m_j}{\rho_j}f\left(\boldsymbol{x}_j\right)W\left(\boldsymbol{x}-\boldsymbol{x}_j,h\right), \end{aligned} \tag{10}$$

or just

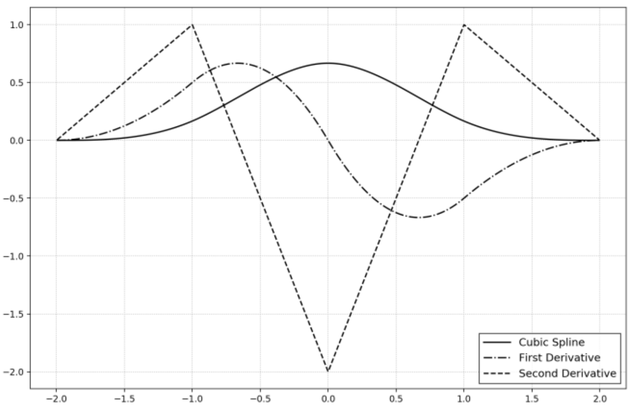

Fig. 12 Cubic spline, h = 1 mm, $\kappa = 2$

$$f\left(\boldsymbol{x}_i\right) \approx \sum_j \frac{m_j}{\rho_j} f\left(\boldsymbol{x}_j\right) W_{ij}, \tag{11}$$

where

$$W_{ij} = W\left(\boldsymbol{x}_i - \boldsymbol{x}_j, h\right). \tag{12}$$

Eq. (11) states that the value of a function at particle i is approximated using the average of those values of the function at all the particles in the support domain of particle i weighted by the smoothing function shown in Fig. 11.

As is obvious from Eq. (11), the resulting value of the field function directly depends on the smoothing function, and also on the current density distribution. Even though the mass m_j is in most cases a constant value taken from the initial particle distribution and density of material, the density ρ_j is not constant in the majority of cases. If the gradients of the density field are not smooth enough, the solution could lead to a pressure field distribution where gradient spikes are present. This is usually a problem when fluid flow is simulated. Since the pressure is an important response in the simulation, it is desirable to obtain a quality pressure field. A density reinitialization scheme (Colagrossi and Landrini 2003, Yreux 2018, Gomez-Gesteira *et al.* 2010), also known as a Shepard filter, was used to gain a smooth density field in this particular case. The density field is updated in such a way that ρ_i becomes

$$\rho_i^{new} = \sum_j \rho_j \tilde{W}_{ij} \frac{m_j}{\rho_j} = \sum_j m_j \tilde{W}_{ij}, \tag{13}$$

where the corrected kernel is expressed as

$$\tilde{W}_{ij} = \frac{W_{ij}}{\sum_j W_{ij} \frac{m_j}{\rho_j}}. \tag{14}$$

Density reinitialization is another operation requiring a certain amount of computational time. Therefore, reinitialization is usually only performed every nth time step, e.g. 20 – 50. For the purpose of comparison, the standard SPH approximation for a density field (Liu and Liu 2003) is expressed as follows

Table 4 Variables and ranges

Φ	0° – 45°
θ	0° – 90°

Table 5 Charge constraints with respect to the centre of the sensor

Δ_{bottom}	100 mm
e_x	0 mm
e_y	0 mm

$$\rho_i = \sum_j m_j W_{ij}. \tag{15}$$

Since density reinitialization is part of the calculation, cubic spline was used as smoothing function. Cubic spline is sufficient since there is an insignificant effect of higher order kernels when blast is simulated. The cubic spline (Liu and Liu 2003) and its first two derivatives are visualized in Fig. 12.

The extent of the support domain is defined according to Fig. 11 as the size of the generally variable parameter h, which is called the smoothing length. Parameter h can also be multiplied by constant κ. In this particular case, initial smoothing length h was 1 mm and $\kappa = 2$.

Particles which are inside the support domain attributable to particle i are called neighbouring particles. If the resultant value of the product κh in each time step of the numerical simulation is the same, there can be the decrease in the number of neighbouring particles and thus also the decrease in the accuracy of the solution due the effect of excessive deformations (i.e. during the mutual divergence of the SPH particles). It is advisable to change the size of the support domain during the calculation in such a way that the number of neighbouring particles is constant.

There are many ways to dynamically develop h so that the number of neighbouring particles remains relatively constant. Benz (1989) suggested a method of developing the smoothing length. This method uses the time derivative of the smoothing function in terms of the continuity equation

$$\frac{dh}{dt} = -\frac{1}{\tilde{d}} \frac{h}{\rho} \frac{d\rho}{dt} = \frac{1}{\tilde{d}} h \nabla \cdot \boldsymbol{v}, \tag{16}$$

where $\tilde{d}$ is the number of dimensions and $\nabla \cdot \boldsymbol{v}$ is the divergence of the flow. This means that the smoothing length increases when particles separate from each other and reduces when the concentration of particles is significant. It varies in order to keep the same number of particles in the neighbourhood. Eq. (16) can be discretized using SPH approximations and calculated with other differential equations in parallel (Liu and Liu 2003).

Due to the Lagrangian nature of the SPH method, interaction with FEM elements was carried out using a penalty-based contact algorithm. More about the interaction can be found in (Husek and Kala 2016).

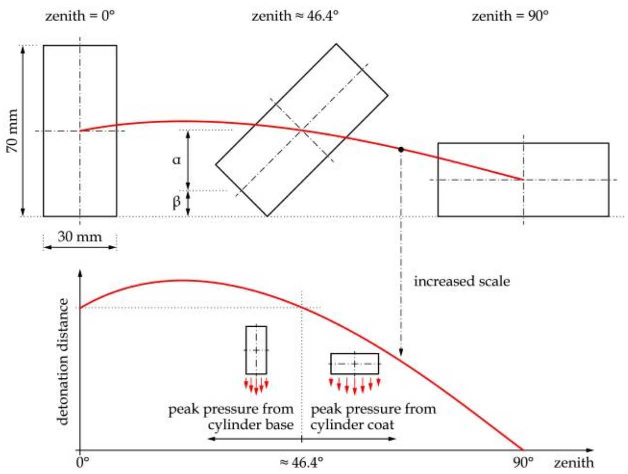

Fig. 13 Detonation distance as a function of zenith angle

4.3 Variables

The influence of the initial rotational deviation of the charge is examined, which requires data on the ranges of several variables. As shown in Fig. 9, two spatial angles are enough to define the initial rotation. Both of the parameters and their ranges are listed in Table 4.

The ranges of the variables were established based on the photo documentation from the experiment, and on Fig. 13. Let us start with the zenith; the value of 0° corresponds to a charge with a perfectly vertical alignment. The maximum zenith was set to 45° for two reasons. First, the photo documentation, from which it is evident that the rotational defect was never higher than 45°. The second reason had a little to do with Fig. 13. Due to several model constraints, the detonation point was also a variable, yet not directly specified. Along with Table 1, where the geometry parameters of the charge are specified, Table 5 provides additional information about the model.

Since the distance between the sensor and the bottom surface of the charge, Δ_{bottom}, was always 100 mm, the distance between the sensor and the detonation point, Δ_{det}, varied with the zenith. The detonation point distance function was expressed as

$$\Delta_{det} = \Delta_{bottom} + \alpha + \beta, \tag{17}$$

where α and β are correction distances based on the length and the diameter. They can be expressed as

$$\alpha = \frac{1}{2} l \cos \Phi, \tag{18}$$

and

$$\beta = \frac{1}{2} d \sin \Phi, \tag{19}$$

where l and d are the length and diameter of the charge. From Eq. (18) and Eq. (19) it can be deduced that when the zenith is 0°, the detonation point distance is Δ_{bottom} plus half of the length. When the zenith is 90°, the detonation point distance is Δ_{bottom} plus half of the diameter. The function of Δ_{det} is, among other things, shown in Fig. 13. In the case where the length and diameter are 70 and 30 mm, respectively, i.e. for a length to diameter ratio of 2.33, the Δ_{det} is identical for 0° and approx. 46.4°. The range was defined according to this fact.

There is yet another reason why the range should not exceed 46.4°, or 45°to be more specific. The schematic visualization in the lower part of Fig. 13 shows that when the cylindrical charge detonates, the pressure field immediately copies the shape of the charge. The pressure peak is, therefore, expected either at the cylinder base or at the cylinder coat. When the charge is vertical, the sensor will detect peak pressure as an outcome of the interaction of flying particles originally located at the cylinder base. The trajectory of such particles is perpendicular to the sensor. When the zenith increases, the angle between the base particles and the sensor is no longer perpendicular. However, when the zenith reaches 90°, the coat particles will have a trajectory which is perpendicular to the sensor. If the zenith is 45°, the angle between the sensor and the trajectory of the base or coat particles is 45°. It theoretically means that for a zenith of 45° the peak pressure will not be as extreme as in any other configuration. Furthermore, since the goal of the paper is not to cover all theoretical variables but only the ones evident from the experiment, a zenith range of 0° to 45° was chosen.

The azimuth plays no role in the detonation point offset since it only defines rotation in the horizontal plane. Therefore, no matter what the value of the azimuth is, the vertical distance of any point of the charge from the sensor is controlled by the zenith only. The azimuth range is only from 0° to 90° due to the symmetry of the sensor (rectangle). Nevertheless, the azimuth plays an important role when force moments at the sensor origin are evaluated.

In Table 5 two other variables, e_x and e_y (constants in this particular case), are mentioned. They are initial eccentricities in the X and Y direction from the detonation point to the centre of the sensor. Since the detonation point is always located in the centre of the charge, the values of 0 mm for both e_x and e_y mean that the detonation point is always located directly above the sensor centre. Examples of several initial distributions for variable zenith and azimuth are shown in Fig. 10.

4.4 Space of designs

To understand the effect of initial rotational deviation a certain number of simulations must be calculated and evaluated. This is a very standard procedure (Kala and Vales 2018, Krejsa *et al*. 2017, Kralik 2017). In statistics, each individual simulation is usually called a design. Every design is generated with respect to given ranges of variables. Together, all designs create what is termed a ‘space of designs’. The question is, what is the most efficient way to generate designs so as to have evenly distributed values and cover all the given ranges? Today, many programs are available for this purpose. One of the best of them is without a doubt optiSLang (Dynardo 2019). Its biggest advantage is its versatility and number of available features. In order to generate a design from a design space, a sampling algorithm has to be chosen. It is a little bit difficult in this case, since the input parameters are angles but the requested design is defined by their product, vector **r**, as shown in Fig. 9. Let us explain this idea further with an example.

The very standard and very well-known Monte Carlo (MC) sampling method (Dynardo 2019) could have been used. Since every design is generated based on the input angles, a point can be projected onto a unit sphere. The point itself is nothing else than the intersection of vector **r** and the unit sphere, as in Fig. 9. The coordinates of the point in the Cartesian system can be calculated from the given angles as

$$\begin{aligned} x &= r\cos\Theta\sin\Phi \\ y &= r\sin\Theta\sin\Phi \\ z &= r\cos\Phi \end{aligned} \tag{20}$$

where r is the radius of the unit sphere, which is 1. The relative coordinates x, y and z can then provide a better understanding of how the charge is oriented in a simulation. As mentioned above, when the MC sampling method is used, the design space may be filled quite well. Yet, when the coordinates are visualized, as shown in Fig. 14, it is obvious that the design space of vector **r** is not filled well. A great quantity of designs are located close to the top of the sphere, while there are very few anywhere else. One could say it is a problem with the Monte Carlo method, and that a more advanced sampling method should be used, e.g. the Latin hypercube sampling (LHS) method (Dynardo 2019). However, when the LHS method is used, the result is more or less the same, as shown in Fig. 15. The question is, where is the root of the problem?

The problem lies in the fact that sampling algorithms have no idea that the design space should be evenly filled with the product of the input parameters, and not the input parameters themselves. For example, many designs were generated on the top of the unit sphere, as is obvious from Fig. 14 and Fig. 15. This means that the zenith as the input parameter was more or less constant, and that the azimuth was evenly filled in within the specified range (0° to 90°). Unfortunately, in this particular case it also means that the product vector **r** is almost identical for every design. Thus, the orientation of the charge is identical as well. There is no meaningful reason why hundreds of almost identical designs should be calculated.

To correct the problem, a tailor-made sampling method has to be created. Yet, it is a very difficult problem to evenly distribute points onto the surface of a sphere. The Fibonacci sphere algorithm (also Fibonacci lattice) can be useful, however (González 2010). Since optiSLang allows Python programming directly inside the program, the Fibonacci sphere algorithm was implemented and used for design generation. The result is shown in Fig. 16. The points (designs) are distributed evenly, which means that, e.g. for a zenith of 0° there is only one simulation. Additionally, 'boundary designs' were generated. These designs correspond to the extreme values of the specified ranges (it is not possible to generate them directly with the Fibonacci sphere algorithm). In this particular case, three designs were generated, as shown in Fig. 10 (the first three simulations from the left). 125 designs were calculated in total in order to achieve a good design space distribution.

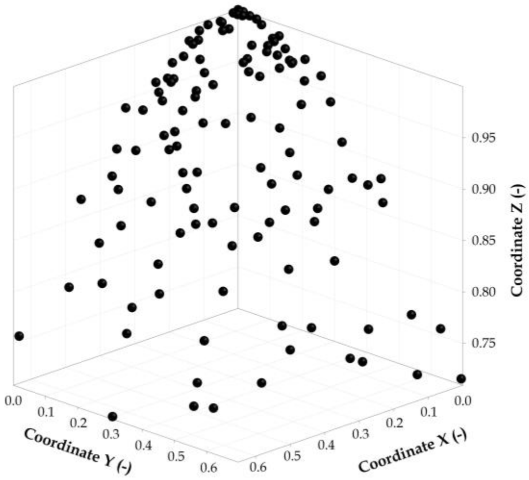

Fig. 14 Monte Carlo sampling

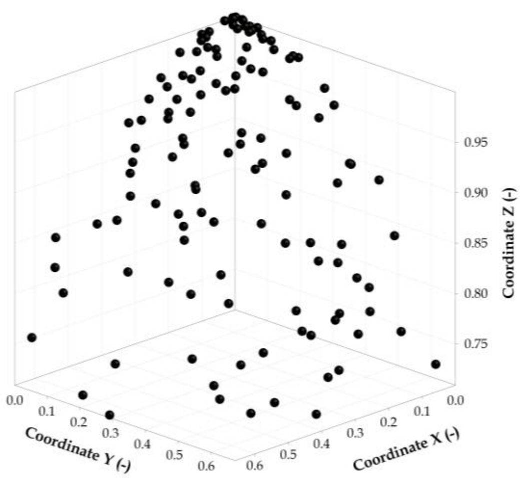

Fig. 15 Latin hypercube sampling

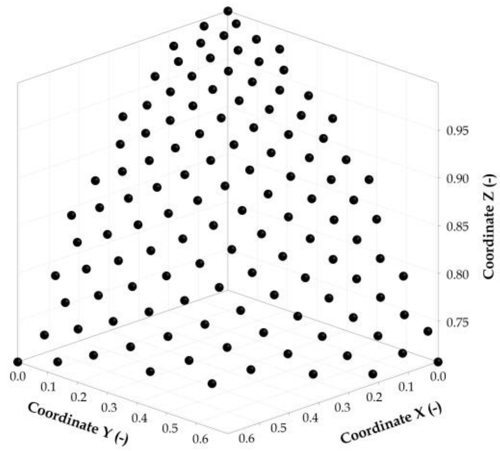

Fig. 16 Fibonacci sphere sampling

5. Results of the numerical simulation

Every calculated design was subjected to automated post-processing, which extracted (among other things) the velocity field of particles, the peak pressure, impulse pressure and pressure distribution on the sensor, the detonation energy released and the reaction components of forces and force moments, as well as total reactions. All of

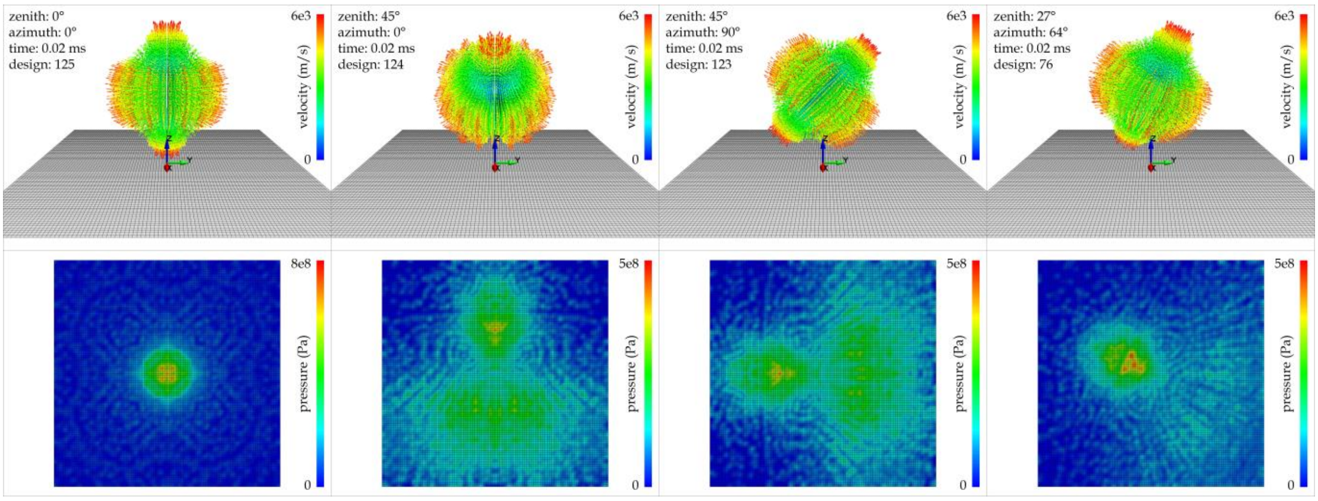

Fig. 17 Numerical simulation overview of three boundary designs (from left) and design 76 (right). Plotted velocity vector field (isometric view) and max pressure distribution over time on the sensor (top view)

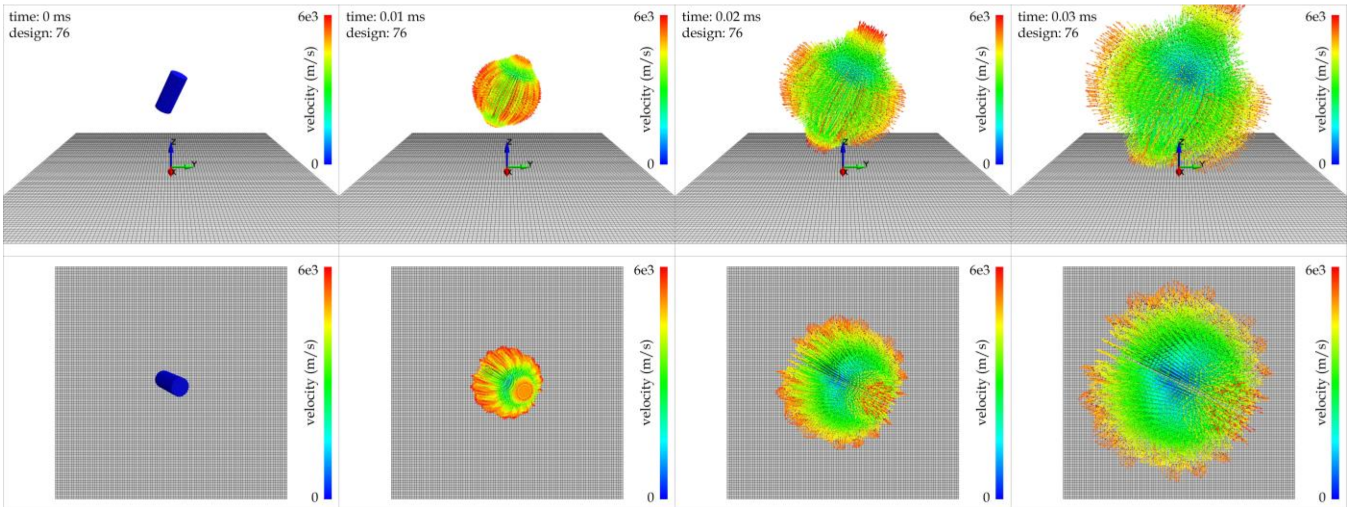

Fig. 18 Time-lapse of the explosion of design 76. Plotted velocity vector field (isometric and top view)

these data were processed in optiSLang, where a metamodel was created for each response. The results obtained for three boundary designs together with design 76 are shown in Fig. 17. In the top part of Fig. 17, the velocity field of particles for each design at time 2 ms is displayed. The maximum particle velocity was approx. 6,000 ms^{-1}, which is, of course, lower than the specified detonation velocity D in Table 2. The reason why the maximum particle velocity is identical for all designs is that the shape, mass, material properties and detonation point were the same for all designs. The only difference can be seen in the max measured pressure over time on the sensor; see the bottom part of Fig. 17. Here the peak pressure differs significantly, as does the pressure distribution, especially when all designs are compared to the design with the zenith equal to 0°. It is important to understand that the peak pressure is a slightly unfortunate response when particle interaction with the FEM is simulated by a penalty-based contact algorithm. The total reaction forces and force moments are of a much greater significance. Nevertheless, the pressure distribution on the sensor does matter because it potentially corresponds to the blackened pattern on the concrete slab from the real experiments. The connection between the pressure distribution and the blackened patterns is discussed later.

The beauty of the SPH method lies in the fact that every particle can be tracked very easily. The exact location of any particle over time, together with the stress field and other characteristics, can provide a great deal of information (compared to MM-ALE or the pressure projection method). In this particular case, the focus should be on the shape or particle distribution of detonation products right after detonation. In Fig. 17 it is quite obvious that a certain shape is formed at that instant. The particles with the maximum velocity values and therefore pressure values are located at the cylinder base and at the cylinder coat, as already mentioned in Fig. 13. A more detailed time-lapse of the design 76 explosion is shown in Fig. 18. When the focus is on the top view, the overall shape of the detonation products is spherical. However, when the focus is on the isometric view, a formed shape is evident, although it also becomes spherical after a certain amount of time. This finding demonstrates why the pressure projection method cannot be

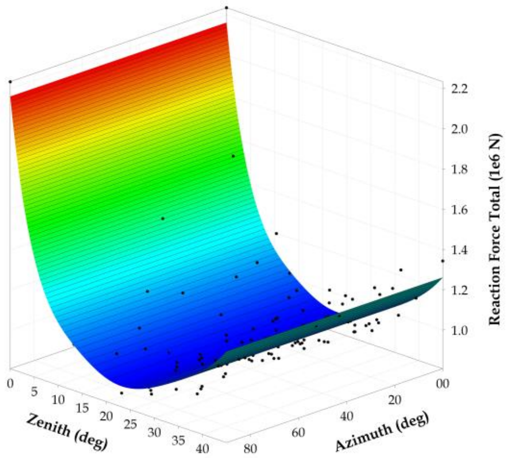

Fig. 19 Moving least squares MOP of total reaction force

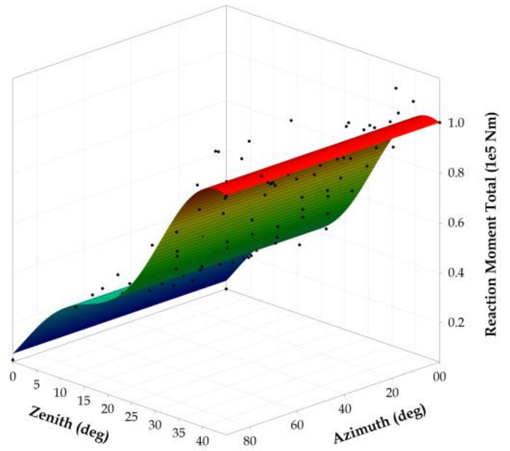

Fig. 20 Isotropic Kriging MOP of total reaction moment

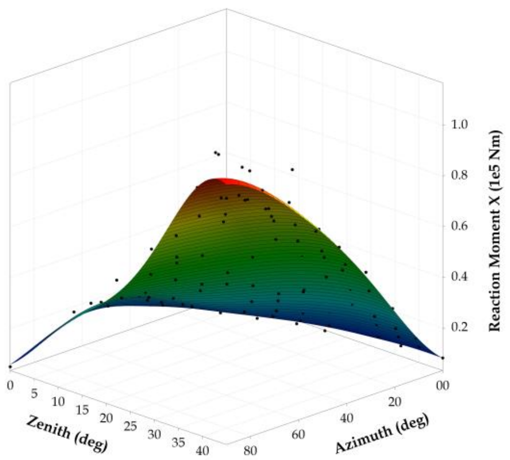

Fig. 21 Isotropic Kriging MOP of reaction moment X

used for close-in detonations when a charge with a certain shape is used.

5.1 Metamodels

When all the simulations have been calculated, approximation models can be created with respect to the

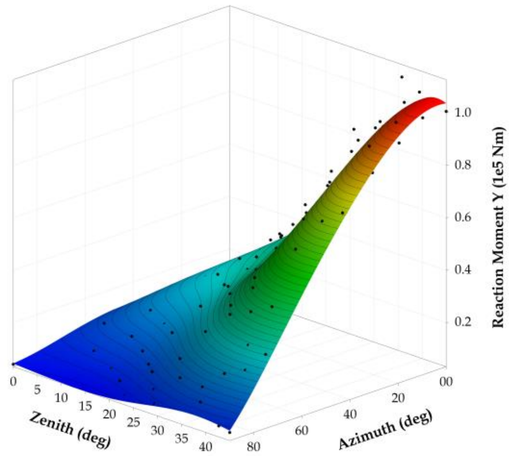

Fig. 22 Isotropic Kriging MOP of reaction moment Y

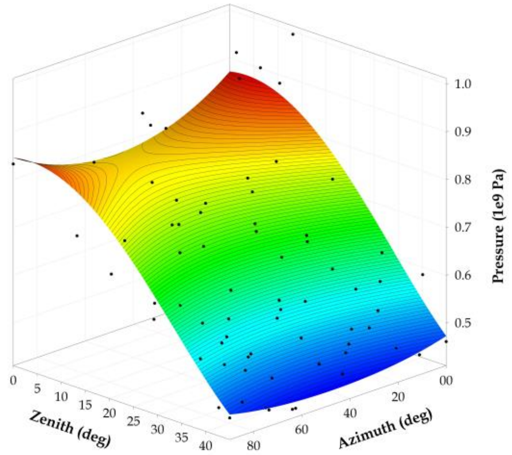

Fig. 23 Linear Regression MOP of pressure

response. Based on these approximation models, conclusions as well as predictions can be made. In optiSLang terminology, an approximation model is referred to as a Metamodel of Optimal Prognosis (MOP) (Dynardo 2019, Most and Will 2008).

The quality of the MOP is quantified with the Coefficient of Prognosis (CoP). The CoP is based on the summation of squared prediction errors. These errors are estimated based on cross validation (Dynardo 2019, Most and Will 2008). The CoP is defined in a range from 0% to 100%, where 100% is the best MOP quality possible. The CoP is influenced by the approximation method. Since it is not the goal of the paper to explain individual methods, Table 6 simply provides an overview of MOPs with respect to the approximation method and the corresponding CoPs.

In Table 6, the prefix *max* specifies that the response was the maximum measured value over time. This is important to keep in mind when two different responses are evaluated, because both could correspond to a different time in the simulation. Since the maximum value was extracted for all responses, the prefix *max* will not be used directly in the text. R_{total} and M_{total} are the total force and total force moment reactions, respectively. Moments M_x and M_y are components of the total force moment reaction with respect

Table 6 Created MOPs with respect to response and approximation method

response	MOP	CoP
$max\ R_{total}$	Moving least squares	97%
$max\ M_{total}$	Isotropic Kriging	95%
$max\ M_x$	Isotropic Kriging	97%
$max\ M_y$	Isotropic Kriging	98%
$max\ P$	Linear Regression	83%

to axis X and Y, and P is the maximum measured pressure. As already mentioned, the interface pressure when particles interact with rigid elements is not something which can be considered to be absolutely reliable. When particles impact the sensor, the contact algorithm is activated. Based on the penetration distance, a virtual spring is created between the penetrating particle and the shell element. The stiffness of the spring is based in the material properties of the interacting parts as well as on the timestep, as is also discussed in (Husek *et al*. 2016). Due to the complexity of the interaction process, the recalculated pressure on the sensor can very often include some artificial pressure spikes. This is also the reason why the quality of the MOP in the case of P is lower than for the other MOPs. In the case of reactions and reaction components, the summation of forces over the sensor for each timestep is calculated (since only one node is fixed, as described in the *Numerical simulation* section). This results in the smoothening of spikes, and better-quality MOP. A visual representation of an MOP for R_{total} is shown in Fig. 19, for M_{total} in Fig. 20, for M_x in Fig. 21, for M_y in Fig. 22, and for pressure P in Fig. 23.

Quite a shocking finding from the MOP of the R_{total} is shown in Fig. 19. When the zenith is 0°, the R_{total} is almost 2,235 kN. When the zenith increases, the charge axis is no longer perpendicular to the sensor and R_{total} drastically drops. When the zenith is approx. 22°, the R_{total} is only 808 kN, which is less than 36% of the maximum force reachable. From the available photo documentation from the experiment, the zenith appears to have been mostly around 15°. A zenith of 15° corresponds to 924 kN, which is only 41% of the R_{total} when the zenith is 0°. In retrospect, when the representative case was calculated, the applied loading in the simulation could have been twice as much as in the experiment, which may have resulted in the calibration failure. Another significant finding is that the azimuth plays a very small, indeed almost insignificant, role when R_{total} is evaluated. It is understandable that for a zenith of 0° the azimuth plays no role. But when the zenith increases, the effect of the azimuth should be evident. However, R_{total} is the sum of all the applied forces on the sensor. It could very well be that in close-in detonations, and in this particular case, all the particles hit the sensor no matter what the azimuth is. This could possibly cause the almost total lack of obvious influence of the azimuth on the R_{total}. The MOP is only an approximation, though. When a detailed comparison is made, design by design, small differences due to changes in the azimuth are evident.

While looking at the MOP of the M_{total} in Fig. 20 it can

Table 7 Force moment values for three boundary designs

Φ	θ	$max\ M_{total}$	$max\ M_x$	$max\ M_y$
0°	0°	0 kNm	0 kNm	0 kNm
45°	0°	100 kNm	0 kNm	100 kNm
45°	90°	100 kNm	100 kNm	0 kNm

Table 8 Input parameters and responses of design 76

Φ	27°
θ	64°
$max\ R_{total}$	977 kN
$max\ M_{total}$	51.8 kNm
$max\ M_x$	32.8 kNm
$max\ M_y$	22.8 kNm
$max\ P$	549 MPa

be seen that the trend compared to that of the MOP of the R_{total} in Fig. 19 is exactly reversed. When the zenith increases, so does the M_{total}. This makes sense, of course, since the centre of the pressure distribution over time is no longer aligned with the centre of the sensor. It is interesting to note that the M_{total} also is not influenced by the azimuth. The reason for this can be found in Fig. 21 and Fig. 22, where the MOPs of M_x and M_y are shown. It might not be obvious but the MOPs of M_x and M_y are mirrored. This can also be seen in Fig. 17 in the case of a zenith of 45° and an azimuth of 0° or 90°. The numbers for the three boundary designs are in Table 7.

It should be noted that absolute values of M_y were used. This was due to the orientation of the coordinate system. For programming purposes, it is easier to work with absolute values of force moment components. It does not change the value of M_{total} since the calculation of M_{total} is based on the Euclidean norm:

$$M_{total} = \sqrt{M_x^2 + M_y^2 + M_z^2}, \tag{21}$$

where M_z is always equal to 0 kNm since the sensor is perpendicular to the Z axis and flying particles have negligible friction when they interact with the sensor. The main outcome from the moment's MOPs is how the asymmetricity of the loading, and therefore the stress distribution and most likely the damage to the concrete slabs, increases with the zenith. This could really be a problem especially when strain gauges are placed in the centre and the maximum measurement is expected, yet it is not obtained.

As already mentioned, when evaluating the peak pressure itself (not the pressure distribution) a certain degree of caution should be maintained. The CoP of the pressure MOP was only 83%, which also points to the fact that due to numerical noise it was not possible to create a better approximation of the response space. The trend of the pressure MOP makes perfect sense, however. When the zenith increases, the peak pressure drops. This occurs because the flying particles impact the sensor at a smaller angle. The smaller the angle, the smaller the normal force from the particle impact. When the zenith is at 45°, the

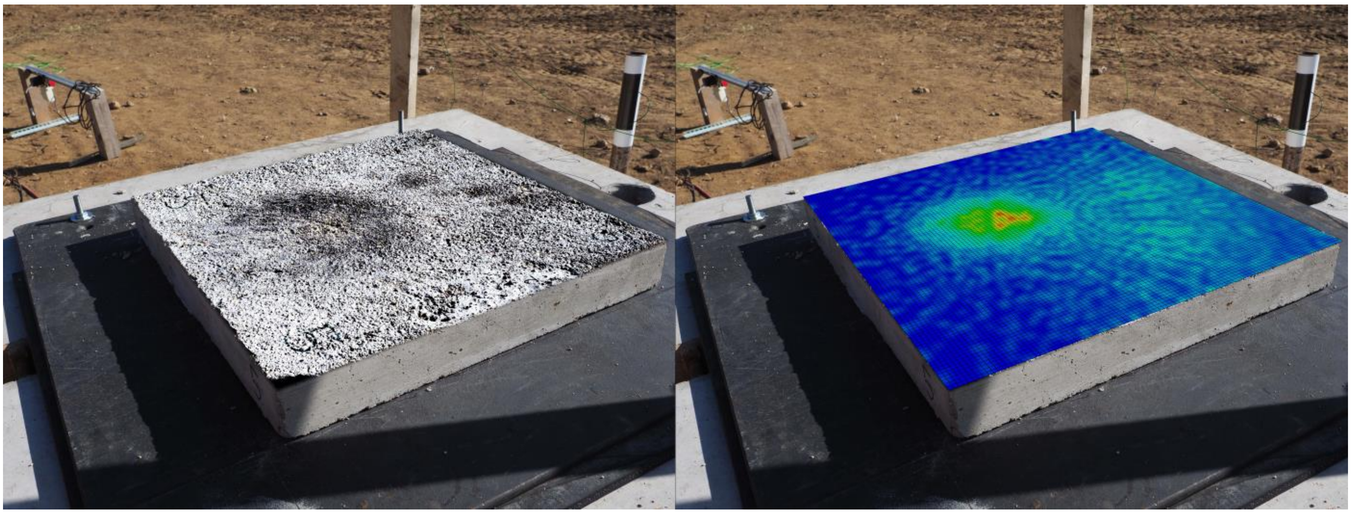

Fig. 24 Comparison of the experiment and calculated design 76

particles with the highest velocity (which probably cause the greatest pressure (as shown in Fig. 13, Fig. 17 and Fig. 18)) impact the sensor at an angle of 45°. When the zenith is higher than 45°, particles originally located at the coat of the cylinder will impact the sensor at a higher angle (getting closer to the perpendicular) and will again cause an increase in pressure. Since the range of the zenith was only to 45°, the mentioned increasing part of the MOP is not visible. The low quality of the pressure MOP is evident when the pressure is evaluated along a constant zenith value. It is to be expected that the pressure is constant when the azimuth changes (as in the case of the R_{total} MOP in Fig. 19). The influence of this numerical noise can be removed, however. The first step is to increase the number of designs. The second step is to apply a filter to achieve pressure field smoothening when post-processing is done. When the pressure spikes are restrained, the quality of an MOP is usually improved (Dynardo 2019, Most and Will 2008).

5.2 Pressure field vs blackened pattern

The MOPs provide a great deal of information. It is possible to see the impact of the input parameters as well as a visualization of the simulated problem. In the section entitled *Incorrect charge placement* an example of an incorrectly placed charge was discussed (shown in Fig. 7). Furthermore, the blackened pattern produced by the incorrectly placed charge was shown in Fig. 8. If the task is to discover which simulated design corresponds to the experiment in Fig. 8, an assumption has to be made. When an explosive detonates, detonation products expand through the air. As discussed, the direction of the expansion is determined by the shape of the charge. Since TNT is a non-ideal explosive its combustion is not complete. It is for this reason that the blackened pattern can be observed at the location through which the blast wave (together with detonation products) would expand if there were no obstacle, i.e. a concrete slab in this particular case. Therefore, the idea of similarity between the experiment and the simulation is based on the comparison of the blackened pattern and the pressure distribution on the sensor. For the purpose of comparison, the same technique as in (Husek and Kala 2018) was used. Using optiSLang, the design most similar to the photograph in Fig. 8 was found. The most similar design is design 76, which has been mentioned several times previously.

The initial configuration is shown along with a time-lapse of the explosion in Fig. 17 and Fig. 18, respectively. The input parameters and responses of design 76 are collected in Table 8.

The R_{total} of design 76 is only 44% of the maximum force reachable (when the zenith is 0°). Of course, this value corresponds to quite an increase in force moment. A comparison of the experiment's blackened pattern and the calculated design 76 is shown in Fig. 24. The pressure distribution shows the maximum pressure reached on the sensor over the simulated time period. In real life, the surface of the concrete slab was white and could only have become darker after the explosion. It is exactly the same in the case of the simulation, but with contours starting from blue. The comparison of both patterns in Fig. 24 looks more than believable.

6. Conclusions

An inside look into experimental measurements followed by numerical simulations and their related uncertainties was presented. The goal of the paper was to show how defects rooted in the experiments can be analysed in numerical simulations. For this purpose, experimental blast loading measurements were used as an example. The experiment itself consisted of a close-in detonation where concrete slabs were subjected to blast. The Smoothed Particle Hydrodynamics (SPH) method was used for the explosion simulation. From the early numerical results, it was obvious that the responses gained from the simulation dramatically differed compared to those from the experimental measurements. This led to the finding that some parameters had not been included in the simulations. After closer observation it was obvious that the rotation of the charge was an experimental defect.

A sensitivity study was carried out, during which the initial rotation was taken into account as a variable. In order to construct metamodels of responses, 125 numerical simulations were calculated and evaluated with optiSLang. The findings show that initial rotation of the charge can potentially cause the total force which is applied to the concrete slabs to significantly differ between measurements. The value of the applied force is not the only problem, however. With increasing initial rotation of the charge, a force moment appears. When the applied load on the concrete slabs is asymmetrical, the measured responses are of no use.

Furthermore, one experimental measurement influenced by the aforementioned defect was analysed in more detail. The corresponding numerical simulation was detected amongst all the simulated designs. The finding shows that the applied force in the experiment conducted on the concrete slab could have been only 50% of the expected force with additional force moment. If experiments like these are to serve as a model for future numerical analyses, it is necessary to consider even the smallest defects that arise during such tests.

Acknowledgments

This outcome has been achieved with financial support from the project GACR 17-23578S ″Damage assessment identification for reinforced concrete subjected to extreme loading″ provided by the Czech Science Foundation.

Nomenclature

capital letters

symbol	description	units
A	linear coefficient of JWL EOS	Pa
B	linear coefficient of JWL EOS	Pa
D	detonation velocity	m/s
E	detonation energy per unit volume	J/m^3
F	burn fraction	–
M_{total}	total force moment reaction	Nm
M_x	component of the total force moment reaction with respect to axis X	Nm
M_y	component of the total force moment reaction with respect to axis Y	Nm
M_z	component of the total force moment reaction with respect to axis Z	Nm
R_1	nonlinear coefficient of JWL EOS	–
R_2	nonlinear coefficient of JWL EOS	–
R_{total}	total force reaction	N
V	relative volume	–
W	smoothing function	–

lowercase letters

symbol	description	units
d	diameter	m
$\tilde{d}$	dimension	–
e_x	eccentricity in X direction	m
e_y	eccentricity in Y direction	m
h	smoothing length	m
l	length	m
m	mass	kg
m_i	mass of SPH particle	kg
p	pressure	Pa
p_{CJ}	Chapman–Jouguet pressure	Pa
p_{eos}	pressure of JWL EOS	Pa
r	radius of unit sphere	–
v	volume of detonation products	m^3
v_0	volume of initial explosive	m^3
x	cartesian relative coordinates in X direction	–
y	cartesian relative coordinates in Y direction	–
z	cartesian relative coordinates in Z direction	–

vectors

symbol	description	units
$\mathbf{x}$	position vector	m
$\mathbf{r}$	direction vector	–
$\mathbf{v}$	velocity vector	m/s

capital Greek letters

symbol	description	units
Δ_{det}	distance between sensor and detonation point of the charge	m
Δ_{bottom}	distance between sensor and bottom surface of the charge	m
ΔV_i	volume of SPH particle	m^3
Ω	integration domain	–

lowercase Greek letters

symbol	description	units
α	correction distance based on the length of the charge	m
β	correction distance based on the diameter of the charge	m
δ	Dirac delta function	–
θ	azimuth	deg
κ	scaling factor of support domain	–
ρ	density of detonation products	kg/m^3
ρ_0	density of initial explosive	kg/m^3
ρ_i	density of SPH particle	kg/m^3
Φ	zenith	deg
ω	nonlinear coefficient of JWL EOS	–

References

Baker, E.L. (1991), "An explosives products thermodynamic equation of state appropriate for material acceleration and overdriven detonation: Theoretical background and formulation", Technical Report ARAED-TR-91013; U.S. Army Armament Research, Development and Engineering Center, USA.

Barsotti, M.A. (2012), "Modeling mine blast with SPH", *Proceedings of the 12th International LS-DYNA Users Conference*, Detroit, USA, June.

Barsotti, M., Sammarco, E. and Stevens, D. (2016), "Comparison of strategies for landmine modeling in LS-DYNA with sandy soil material model development", *Proceedings of the 14th International LS-DYNA Users Conference*, Detroit, USA, June.

Benz, W. (1989), "Smoothed particle hydrodynamics: A review", NATO Workshop NATO Workshop, Les Arcs, France.

Codina, R., Ambrosini D. and Borbon, F. (2016), "Experimental and numerical study of a RC member under a close-in blast", *Eng. Struct.*, **127**, 145-158. https://doi.org/10.1016/j.engstruct.2016.08.035.

Colagrossi, A. and Landrini, M. (2003), "Numerical simulation of interfacial flows by smoothed particle hydrodynamics", *J. Comput. Phys.,* **191**(2), 448-475. https://doi.org/10.1016/S0021-9991(03)00324-3.

Dynardo (2019), *Methods for Multi-Disciplinary Optimization and Robustness Analysis*, Dynardo GmbH, Weimar, Germany.

Gomez-Gesteira, M., Rogers, B.D., Dalrymple, R. and Crespo, A.J.C. (2010), "State-of-the-art of classical SPH for free-surface flows", *J. Hydraulic Res.*, **48,** 6-27. https://doi.org/10.1080/00221686.2010.9641242.

González, Á. (2010), "Measurement of areas on a sphere using fibonacci and latitude–longitude lattices", *Math. Geosci.,* **42**, 49-64. https://doi.org/10.1007/s11004-009-9257-x.

Han-Gul, G. and Hyo-Gyoung, K. (2017), "A tensile criterion to minimize FE mesh-dependency in concrete beams under blast loading", *Comput. Concrete,* **20**(1), 1-10. https://doi.org/10.12989/cac.2017.20.1.001.

Hilding, D. (2016), "Methods for modelling air blast on structures in LS-DYNA", *Proceedings of the Nordic LS-DYNA Users' Conference*, Gothenburg, Sweden, June.

Husek, M. and Kala J. (2016), "Improved element erosion function for concrete-like materials with the SPH method", *Shock Vib.,* **2016**, 1-13. http://dx.doi.org/10.1155/2016/4593749.

Husek, M., Kala, J., Kral, P. and Hokes, F. (2016), "Concept and numerical simulations of a reactive anti-fragment armour layer", *Proceedings of the 14th International Conference of Numerical Analysis and Applied Mathematics*, Rhodes, Greece, September.

Husek, M. and Kala, J. (2018), "Material structure generation of concrete and its further usage in numerical simulations", *Struct. Eng. Mech.*, **68**(3), 335-344. https://doi.org/10.12989/sem.2018.68.3.335.

Chen, J.Y and Lien, F.S. (2018), "Simulations for soil explosion and its effects on structures using SPH method", *J. Impact Eng.,* **112**, 41-51. https://doi.org/10.1016/j.ijimpeng.2017.10.008.

Jin-Won, N., In-Seok Y. and Seong-Tae Y. (2016), "Numerical evaluation of FRP composite retrofitted reinforced concrete wall subjected to blast load", *Comput. Concrete*, **17**(2), 215-225. https://doi.org/10.12989/cac.2016.17.2.215.

Jin, M., Haoa, Y. and Haoc, H. (2019), "Numerical study of fence type blast walls for blast load mitigation", *J. Impact Eng.*, **131**, 238-255. https://doi.org/10.1016/j.ijimpeng.2019.05.007.

Jun, L. and Hong, H. (2014), "Numerical study of concrete spall damage to blast loads", *J. Impact Eng.*, **68**, 41-55. https://doi.org/10.1016/j.ijimpeng.2014.02.001.

Kala, Z. and Vales, J. (2018), "Imperfection sensitivity analysis of steel columns at ultimate limit state", *Arch. Civil Mech. Eng.,* **18**(4), 1207-1218. https://doi.org/10.1016/j.acme.2018.01.009.

Kralik, J. (2017), "Probability and sensitivity nonlinear analysis of the hermetic cover of main shut-off valve under extreme pressure and temperature", *Civil Engineering Series,* **17**(1), 96-111.http://hdl.handle.net/10084/122558.

Krejsa, M., Koubova, L., Flodr, J., Protivinsky, J., Thanh, Q.N. (2017), "Probabilistic prediction of fatigue damage based on linear fracture mechanics", *Frattura ed Integrita Strutturale,* **39**(1), 143-159. https://doi.org/10.3221/IGF-ESIS.39.15.

Kurtoglu, I., Salihoglu, B., Tasan, Y.C. and Tekin, G. (2013), "Validation of mine blast simulations with field tests", *Proceedings of the 9th LS-DYNA Conference*, Manchester, United Kingdom, June.

Le Blanc, G., Adoum, M. and Lapoujade, V. (2005), "External blast load on structures – Empirical approach", *Proceedings of the 5th European LS-DYNA Users Conference*, Birmingham, UK, May.

Lin, S.Ch., Li, D. and Yang, B. (2019), "Experimental study and numerical simulation on damage assessment of reinforced concrete beams", *J. Impact Eng.*, **132,** 1-15. https://doi.org/10.1016/j.ijimpeng.2019.103323.

Liu, G.R. (2010), *Meshfree Methods – Moving Beyond The Finite Element Method*, CRC Press, Boca Raton, Florida, USA.

Liu, G.R. and Liu M.B. (2003), *Smoothed Particle Hydrodynamics: A Meshfree Particle Method*, World Scientific Publishing Co. Pte. Ltd., Singapore.

Liu, G.R. and Liu M.B. (2010), "Smoothed particle hydrodynamics (SPH): An overview and recent developments", *Arch. Comput. Methods in Eng.*, **17,** 25-76. https://doi.org/10.1007/s11831-010-9040-7.

LSTC (2019a), *LS-DYNA Theory Manual*, Livermore Software Technology Corporation, Livermore, California, USA.

LSTC (2019b), *LS-DYNA Keyword User's Manual - Volume II: Material models*, Livermore Software Technology Corporation, Livermore, California, USA.

Luccioni, B., Aráoz, G. (2011), "Erosion Criteria for Frictional Materials Under Blast Load", *Mecánica Computacional,* **XXX**(21), 1809-1831. https://cimec.org.ar/ojs/index.php/mc/article/view/3868.

Luccioni, B., Isla, F., Codina, R., Ambrosini, D., Zerbino, R., Giaccio, G. and Torrijose, M.C. (2017), "Effect of steel fibers on static and blast response of high strength concrete", *J. Impact Eng.,* **107**, 23-37. https://doi.org/10.1016/j.ijimpeng.2017.04.027.

Monaghan, J.J. (1992), "Smoothed particle hydrodynamics", *Annual Review Astronomy Astrophys.*, **30**, 543-574. https://doi.org/10.1146/annurev.aa.30.090192.002551.

Most, T. and Will, J. (2008), "Metamodel of optimal prognosis – an automatic approach for variable reduction and optimal metamodel selection", *Proceedings of the Weimarer Optimierungs- und Stochastiktage 5.0*, Weimar, Germany, November.

Murray, Y.D. (2007), "User's Manual for LS-DYNA Concrete Material Model 159", Report No. FHWA-HRT-05-062; U.S. Department of Transportation, Federal Highway Administration, McLean, Virginia.

Murray, Y.D., Abu-Odeh, A. and Bligh, R. (2007), "Evaluation of Concrete Material Model 159", Report No. FHWA-HRT-05-063; U.S. Department of Transportation, Federal Highway Administration, McLean, Virginia.

Rashad, M. and Yang, T.Y. (2019), "Improved nonlinear modelling approach of simply supported PC slab under free blast load using RHT model", *Comput. Concrete*, **23**(2), 121-131. https://doi.org/10.12989/cac.2019.23.2.121.

Rashad, M., Wahab, M.M.A. and Yang, T.Y. (2019), "Experimental and numerical investigation of RC sandwich panels with helical springs under free air blast loads", *Steel Compos. Struct.*, **30**, 217-230.https://doi.org/10.12989/scs.2019.30.3.217.

Ruggiero, A., Bonora, N., Curiale, G., Muro, S.D, Iannitti, G., Marfia, S., Sacco, E., Scafati, E. and Testa, G. (2019) "Full scale experimental tests and numerical model validation of reinforced concrete slab subjected to direct contact explosion", *J. Impact Eng.*, **132**, 1-15. https://doi.org/10.1016/j.ijimpeng.2019.05.023.

Shi, Y., Stewart, M.G. (2015), "Damage and risk assessment for reinforced concrete wall panels subjected to explosive blast loading", *J. Impact Eng.*, **85**, 5-19. https://doi.org/10.1016/j.ijimpeng.2015.06.003.

Schwer, L. (2010), "A Brief Introduction to coupling load blast enhanced with multi-material ALE: The best of both worlds for air blast simulation", *Proceedings of the 9th LS-DYNA Forum*, Bamberg, Germany, October.

Schwer, L., Teng, H. and Souli, M. (2015), "LS-DYNA air blast techniques: Comparison with experiments for close-in charges", *Proceedings of the 10th European LS-DYNA Conference*, Würzburg, Germany, June.

Slavik, T.P. (2009), "A coupling of empirical explosive blast loads to ALE air domains in LS-DYNA", *Proceedings of the 7th European LS-DYNA Conference*, Salzburg, Austria, May.

Sohn, J.M., Kim, S.J., Seong, D.J., Kim, B.J., Ha, Y.Ch., Seo, J.K. and Paik, J.K. (2014), "Structural impact response characteristics of an explosion- resistant profiled blast walls in arctic conditions", *Struct. Eng. Mech.*, **51**(5), 755-771. https://doi.org/10.12989/sem.2014.51.5.755

Toussaint, G. and Bouamoul, A. (2010), "Comparison of ALE and SPH methods for simulating mine blast effects on structures", Technical Report TR 2010-326; Defence Research and Development Canada, Valcartier, Canada.

Toussaint, G. and Durocher, R. (2008), "Finite element simulation using SPH particles as loading on typical light armoured vehicles", *Proceedings of the 10th International LS-DYNA Users Conference*, Detroit, USA, June.

Trajkovski, J. (2017), "Comparison of MM-ALE and SPH methods for modelling blast wave reflections of flat and shaped surfaces", *Proceedings of the 11th European LS-DYNA Conference*, Salzburg, Austria, May.

Tuan N. and Priyan M. (2009), "Modelling the dynamic response and failure modes of reinforced concrete structures subjected to blast and impact loading", *Struct. Eng. Mech.*, **32**(2), 269-282. https://doi.org/10.12989/sem.2009.32.2.269

US Army (1986), "Fundamentals of protective design for conventional weapons", Technical Manual TM 5-855-1; Headquarters, Department of the Army, USA.

US Army (1990), "Structures to resist the effects of accidental explosions", Technical Manual TM 5-1300; Departments of the Army, the Navy, and the Air Force, USA.

Will, J. and Eckardt, S. (2017), "Optimization of Hydrocarbon Production from Unconventional Shale Reservoirs using Numerical Modelling", *J. Petroleum Technol.*, **4,** 14-23. http://dx.doi.org/10.15377/2409-787X.2017.04.01.3

Will, J., Eckardt, S. and Ranjan, A. (2017), "Numerical Simulation of Hydraulic Fracturing Process in an Enhanced Geothermal Reservoir using a Continuum Homogenized Approach", *Procedia Engineering of Symposium of the International Society for Rock Mechanics of the EUROCK 2017*, Ostrava, Czech Republic, July. https://doi.org/10.1016/j.proeng.2017.05.249

Wua, Z., Zhangb, P., Fana, L. and Liua, Q. (2019), "Debris characteristics and scattering pattern analysis of reinforced concrete slabs subjected to internal blast loads – A numerical study", *J. Impact Eng.*, **131**, 1-16. https://doi.org/10.1016/j.ijimpeng.2019.04.024

Xiao, W., Andrae, M., Gebbeken, N. (2019), "Experimental and numerical investigations on the shock wave attenuation performance of blast walls with a canopy on top", *J. Impact Eng.*, **131**, 123-139. https://doi.org/10.1016/j.ijimpeng.2019.05.009

Yreux, E. (2018), "Fluid flow modeling with SPH in LS-DYNA", *Proceedings of the 15th International LS-DYNA Users Conference*, Detroit, USA, June.

Yun, S.H., Jeon, H.K. and Park, T. (2013), "Parallel blast simulation of nonlinear dynamics for concrete retrofitted with steel plate using multi-solver coupling", *J. Impact Eng.*, **60**, 10-23. https://doi.org/10.1016/j.ijimpeng.2013.04.001

Yuan, S., Hao, H. and Zong, Z. (2017), "A study of RC bridge columns under contact explosion", *J. Impact Eng.,* **109**, 378-390. https://doi.org/10.1016/j.ijimpeng.2017.07.017

Zhan, L., Li, Ch., Qin, F., Wensu Ch., Hong, H., Rong, Z. and Kang, Z. (2019), "Experimental and numerical study on CFRP strip strengthened clay brick masonry walls subjected to vented gas explosions", *J. Impact Eng.*, **129**, 66-79. https://doi.org/10.1016/j.ijimpeng.2019.02.013

PL